nature communications

Article

https://doi.org/10.1038/s41467-025-56542-1

Precession modulates the poleward expansion of atmospheric circulation to the Arctic Ocean

Received: 12 September 2024

Accepted: 21 January 2025

Published online: 29 January 2025

Check for updates

Yi Zhong[1,2] ✉, Zhengyao Lu[3,4] ✉, Stefanie Kaboth-Bahr[5], Jimin Yu[6,7,8], Keiji Horikawa[9], Mark J. Dekkers[10], Juan C. Larrasoaña[11,12], Peter D. Clift[13], Michael E. Weber[14], Flor Vermassen[15], Sev Kender[16], Chijun Sun[17], Hu Yang[18], Xianfeng Wang[19], Camilla S. Andresen[20], Yanguang Liu[21,22], Haiwei Zhang[23], Zhengyang Dai[1], Lu Niu[24], Jingyu Zhang[1], Xuguang Feng[21], Debo Zhao[25], Wenyue Xia[1], Sheng Yang[1], Hai Li[26] & Qingsong Liu[1,27] ✉

Under sustained global warming, Arctic climate is projected to become more responsive to changes in North Pacific meridional heat transport as a result of teleconnections between low and high latitudes, but the underlying mechanisms remain poorly understood. Here, we reconstruct subarctic humidity changes over the past 400 kyr to investigate the role of low-to-high latitude interactions in regulating Arctic hydroclimate. Our reconstruction is based on precipitation-driven sediment input variations in the Subarctic North Pacific (SANP), which reveal a strong precessional cycle in subarctic humidity under the relatively low eccentricity variations that dominated the past four glacial-interglacial cycles. Combined with climate model simulations, we highlight that precession drives meridional shifts in the northern rim of the North Pacific Subtropical Gyre (NPSG) and modulates the efficiency of heat and water vapor transfer to the SANP and Arctic regions. Our findings suggest that projections of a northward shift of the NPSG in response to future global warming will lead to wetter conditions in the Arctic Ocean and enhanced sea-ice loss.

Traditionally, the ongoing Arctic warming has been thought to be accelerated by decreases in surface albedo associated with melting ice and snow[1,2] caused by radiative forcing from high CO_2 emission[3,4]. However, a recent high-resolution model study highlights that the impact of ocean heat and moisture transport through the Bering Strait likely on Arctic warming is bigger than that of CO_2 emission[5]. Thus, poleward heat and moisture transport from the low-latitude North Pacific regions is potentially a critical factor in regulating climate and sea-ice extent in the Arctic[6,7]. Poleward heat and moisture transport by the ocean and atmosphere operates across the mid-latitudes of the Pacific, with the ocean transferring ~70% of the heat to the atmosphere between 25°N and 45°N[8,9]. Mid-to-high latitude ocean gyres of the North Pacific Ocean[10], then redistribute the heat and moisture to the Arctic Ocean[8]. While a potential link exists between the modern transport of heat/moisture from the North Pacific Subtropical Gyre (NPSG) and the climate in the Arctic, mechanisms driving this poleward transport of heat and moisture in the North Pacific during glacial-interglacial cycles, the processes driving its variability, and their impact on Arctic sea-ice extent, remain poorly understood[9]. This lack of understanding is partly a result of the absence of long-term and high-resolution humidity records from the Bering Sea, which is critical to heat and moisture transport to the Arctic Ocean.

The Bering Sea, located in the Subarctic North Pacific (SANP), is connected with the Arctic Ocean through the Bering Strait (sill depth ~50 m). The Alaska Coastal Current transports heat to the Arctic Ocean via the Bering Sea[11]. We analysed clay and magnetic minerals of marine sediment cores obtained at Integrated Ocean Drilling Program (IODP) Site U1342 (54.83°N, 176.92°E, 818-m water depth) drilled on Bowers

A full list of affiliations appears at the end of the paper. ✉e-mail: zhongy@sustech.edu.cn; zhengyao.lu@nateko.lu.se; qsliu@sustech.edu.cn

Ridge in the Bering Sea during Expedition 323 (Fig. 1), and reconstructed continental humidity records for the past 400 kyr (Supplementary Figs. 1, and 2). Analysis of reconstructed poleward heat and moisture transport from the NPSG to the Arctic Ocean (Fig. 1), along with model simulations, offers insights into mechanisms controlling Arctic sea-ice extent and high-latitude ocean-atmosphere dynamics, with important implications for future Arctic responses to ongoing global warming.

Results and discussion

Orbital changes in North Pacific precipitation

A ternary diagram of clay mineral composition (smectite, illite, chlorite + kaolinite wt%) of sediments from Site U1342 shows that most glacial and interglacial sediments resemble those from the Eastern Aleutian Basin (Supplementary Fig. 3). The clay minerals deposited at Site U1342 were likely sourced from the Aleutian Arc region, adjacent to the Eastern Aleutian Basin[12] (Supplementary Fig. 1b). We focus on goethite, a magnetic mineral which currently forms in soils under relatively humid conditions (i.e., precipitation exceeding evaporation) and cool, less seasonal conditions[13,14]. The dominant magnetic mineral in Bering Sea deep-sea sediments recovered from Site U1342 is detrital magnetite, and the overall rock magnetic variability is known to be essentially minimally altered by early diagenesis in Bering Sea deep-sea sediments[15,16]. As a result, we consider variations in goethite concentration in sediments from Site U1342 a reliable proxy for past moisture changes in the Aleutian Arc region.

This high-resolution goethite content record spanning the past 400 kyr (Fig. 2e) shows significant 67-kyr and 23 kyr periodicities (Fig. 3a, b). The former is suggested to reflect a nonlinear variability in the Bering Sea climate system during the late Quaternary[17], influenced by the interactions between the high-latitude 100-kyr cycle and the 41-kyr obliquity cycle. We note that the same cyclicity has also been reported in the planktonic foraminiferal $\delta^{18}O$ record from Site U1312 in the mid-latitude North Atlantic[18]. The cyclicity found at IODP Site U1312 may have been influenced by both low-latitude North Atlantic (sub) surface water changes[19] and the expansion of Northern Hemisphere ice sheets. Similarly, the ~67-kyr periodicity found in the goethite record of Site U1342 might be the result of the interactions between high-latitude ice-sheet dynamics and low-latitude heat-moisture forcing in the North Pacific.

The clear 23 kyr precession signal in Site U1342 is also mirrored by a composite Arctic Palaeoclimate Index (API) stack from benthic foraminiferal and ostracod density from central Arctic Ocean sediment cores (Fig. 2f)[20]. High spectral density is associated with high productivity and low sea-ice extent (Fig. 2f)[20] during warm periods with dominant responses on the eccentricity and precession band (Fig. 3c)[21]. If we ignore longer cycles in the Arctic Ocean records, the density variations suggest that poleward transport of heat and moisture over the western SANP and central Arctic was driven by precession-forced low-latitude climate change. This aligns with recent model simulations, which show that precession plays a dominant role in Arctic sea-ice formation, linked to the response of local summer insolation and northward oceanic heat transport[22,23].

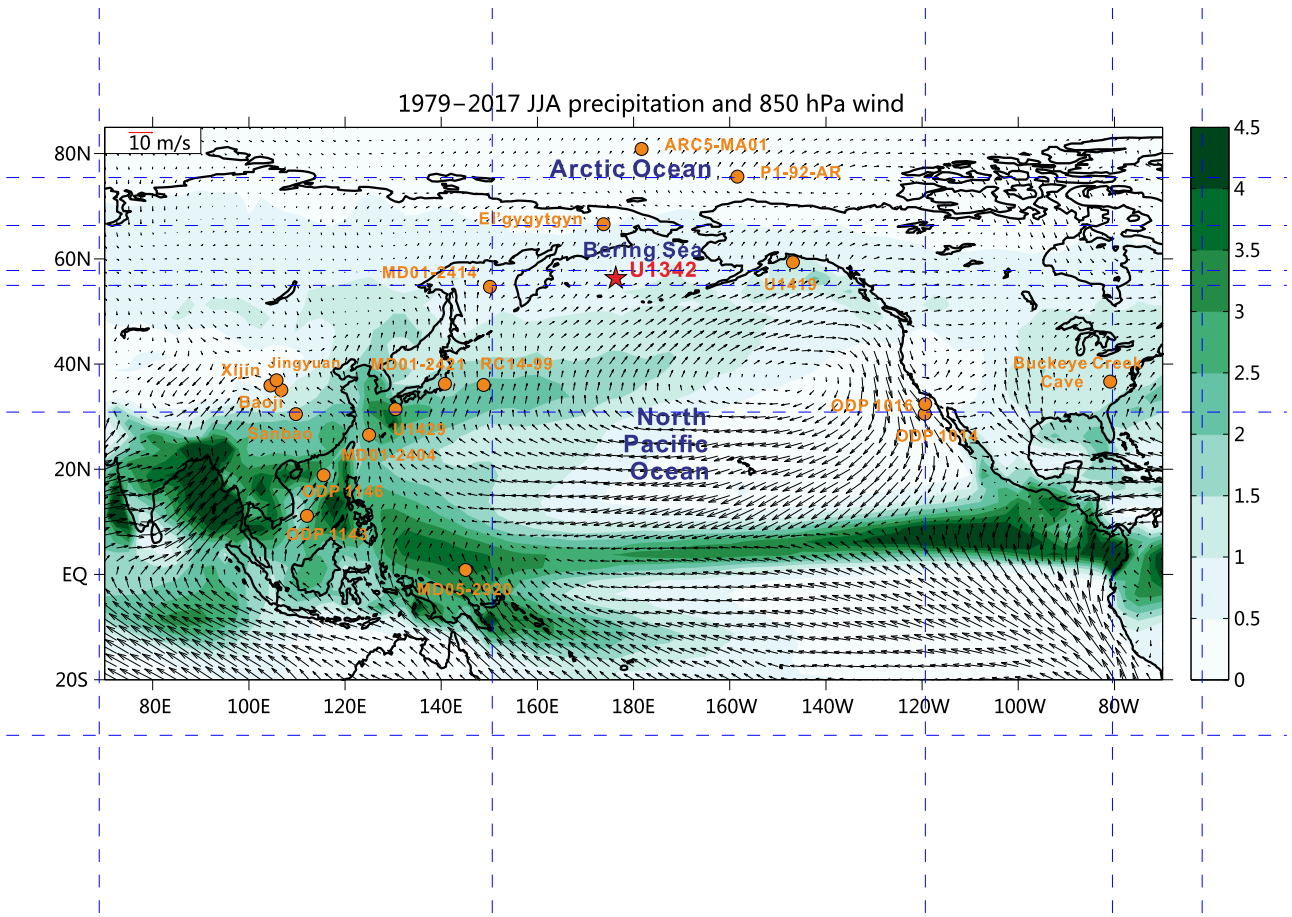

Fig. 1 | Regional map showing annual mean precipitation (color shading; see scale bar) and 850 hPa winds (arrows), based on the NCEP-DOE reanalysis (1979–2017)[87]. Marine records include IODP Site U1342 (this study), ARC5-MA01[36], P1-92-AR[21], U1419[88], RC14-99[89], MD01-2421[90], MD01-2404[91], U1429[25] in the North Pacific, ODP Site 1146[92], ODP Site 1143[93] in the South China Sea and MD05-2920 in the central Pacific Ocean[94]. Terrestrial records include the loess sequences from Jingyuan[95], Xijin[96], and speleothem records from Sanbao[27] and Buckeye Creek Cave[28]. Information on the locations of these sites is summarized in Supplementary Table 1.

https://doi.org/10.1038/s41467-025-56542-1

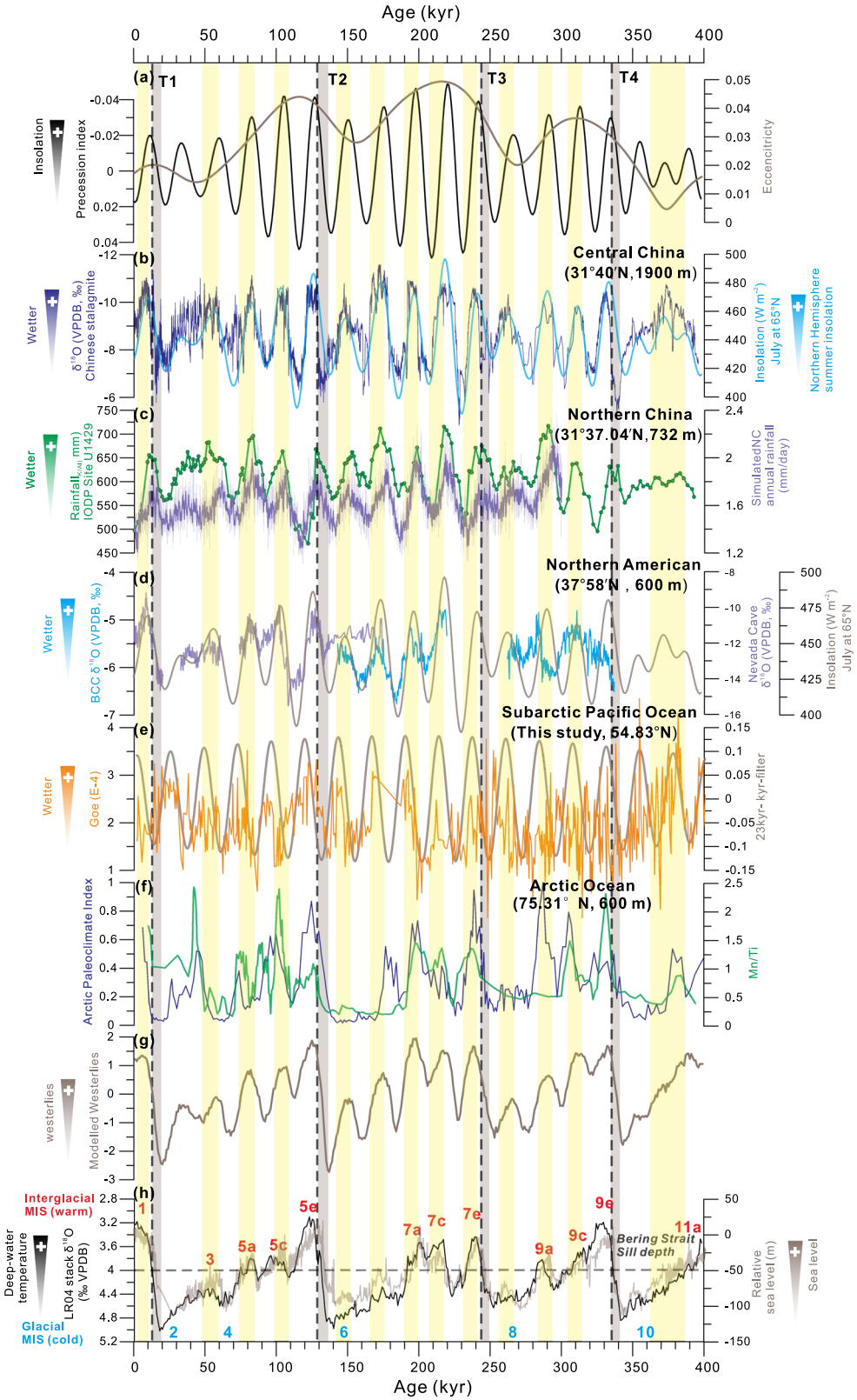

Fig. 2 | Rainfall records from the high and low latitude Pacific Ocean since 400 ka. a Precession and eccentricity[37]; **b** Chinese cave stalagmite $\delta^{18}O$ record from Sanbao[27] and Northern Hemisphere summer insolation (65°N, July-September)[37]; **c** North China rainfall changes based on K/Al at IODP Site 1429 (green) and simulations (purple)[24]; **d** Buckeye Creek Cave $\delta^{18}O$ record[28] and July insolation at 65°N[37]; **e** Goethite contents in IODP Site U1342 (this study) and 23 kyr (thick gray line) Gaussian bandpass filtered output; **f** Arctic Paleoclimate Index[20] and Mn/Ti from ARC5-MA01[38]; **g** Simulated annual mean North Pacific westerlies (35°N-55°N, 120°E-240°E), normalized at 500 hPa[46]; **h** LR04 benthic $\delta^{18}O$ stack[74] and global sea-level[97]. The gray and yellow vertical bars mark glacial terminations and orbital periodicities, respectively.

https://doi.org/10.1038/s41467-025-56542-1

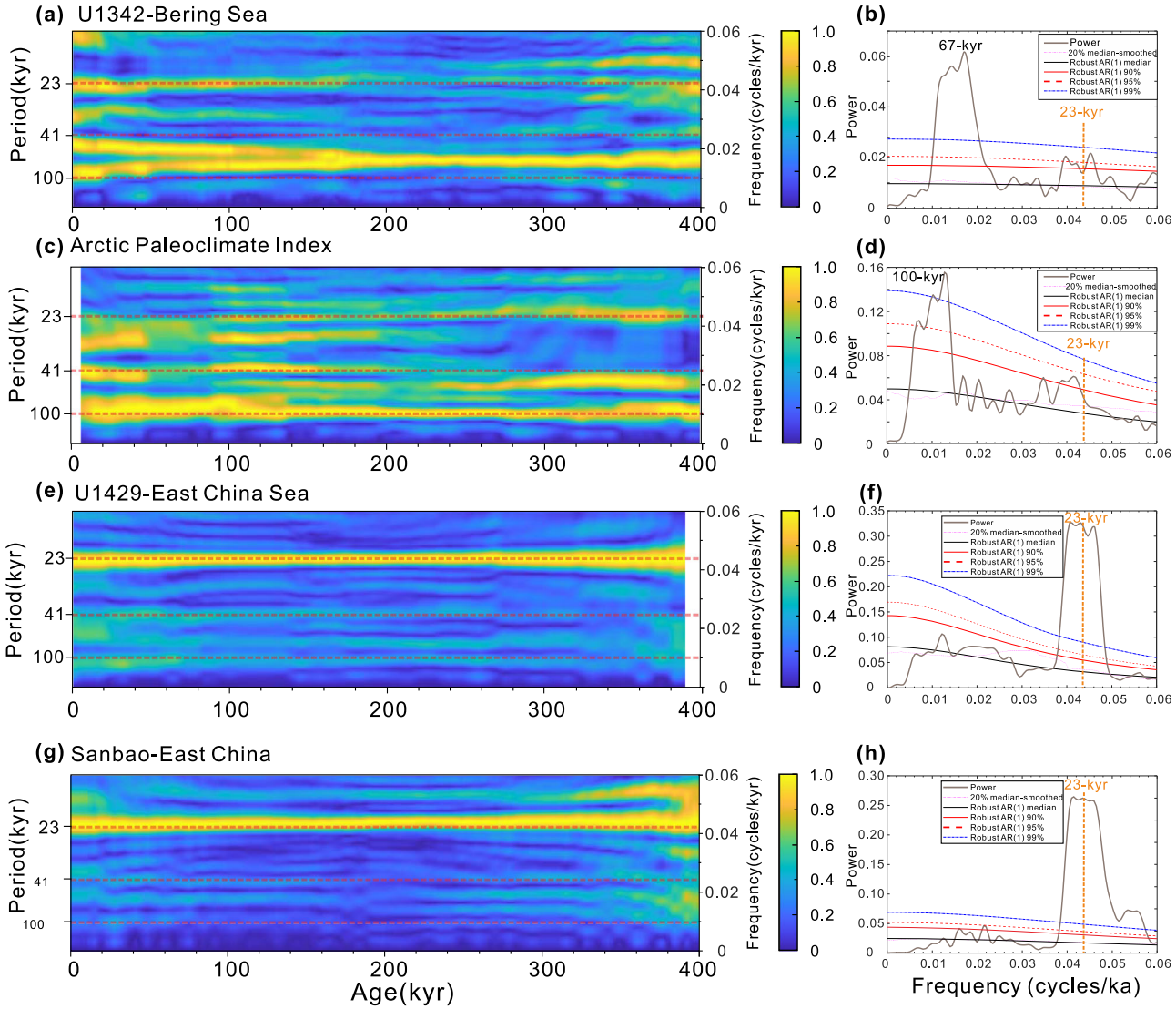

Fig. 3 | Orbital-scale climate variability during the last 400 kyr. Evolutive spectra of **a** Goethite content at IODP Site U1342 (this study), **c** Arctic Palaeoclimate Index[20], **e** K/Al at IODP Site U1429[25], and **g** Chinese stalagmite $\delta^{18}O$ record[27]. Power spectrum analyses of **b** Goethite contents in IODP Site U1342 (this study), **d** Arctic Palaeoclimate Index[20], **f** K/Al in IODP Site U1429[26], and **h** Chinese stalagmite $\delta^{18}O$ record[27]. Orange dashed lines indicate significant peaks at the period of 23 kyr.

Interestingly, the precession signal in the SANP is evident at ~0–200 ka and ~320–400 ka, as revealed by the evolutive spectra, but appears weaker between 200 and 320 ka (Fig. 3a). Precipitation records from the low- to mid-latitudes across the North Pacific region consistently exhibit a precession signal throughout the last 400 kyr, as documented in the East China Sea[24–26] (Fig. 2c), central and eastern China[27] (Fig. 2b) and North America[28,29] (Fig. 2d), with higher precipitation correspond to lower precession. In general, wetter conditions coincide with higher boreal summer insolation[30] (Fig. 2a). Compared to wavelet changes from low- and mid-latitude records (Fig. 3e-h), the co-occurrence of strong ~67-kyr and ~23-kyr cycles in our goethite content record (Fig. 3a) implies that moisture changes in the high-latitude Pacific are influenced by both precession and glacial boundary conditions[31,32].

Coupling mechanism between high and low latitude moisture transport

The goethite record from Site U1342 suggests that the precessional signal within subarctic humidity is only expressed at eccentricity minima during the past 400 kyr (Fig. 2a, e). Despite its small net effect on the annual mean insolation, eccentricity exerts a strong modulation on insolation amplitude changes by affecting precession[33]. For example, eccentricity forcing was observed in African moisture patterns, indicating that low-latitude insolation processes governed Eastern African regional precipitation[34,35]. Some model simulations also predicted that Northern Hemisphere ice sheets increased in size, with their southern extent reaching lower latitudes during periods of lower eccentricity[36]. Thus, these precession-driven precipitation changes, modulated by eccentricity, may have influenced high-latitude ice-sheet build-up during MIS 2-4 and MIS 12 which featured the most intense glaciations over the past 400 kyr (Fig. 2h)[37].

Based on this evidence, we interpret that the SANP area became more sensitive to low-latitude precession-driven summer insolation changes during eccentricity minima. For example, under precession maxima and eccentricity minima, the expansion of the North Pacific gyre strengthens the poleward heat and moisture transport to high latitudes. Overall, strong precession signals[38] (Fig. 2a) are consistent with high Arctic palaeoclimate proxy records, including Mn/Ti ratios (Fig. 2f)[39], color reflectance, bulk density, rock magnetic properties, and microfossil abundance over this time period[20,40–42]. This implies that even though precessional forcing is commonly associated with low-latitude processes[27], specifically in driving the Asian monsoon[27,43],

https://doi.org/10.1038/s41467-025-56542-1

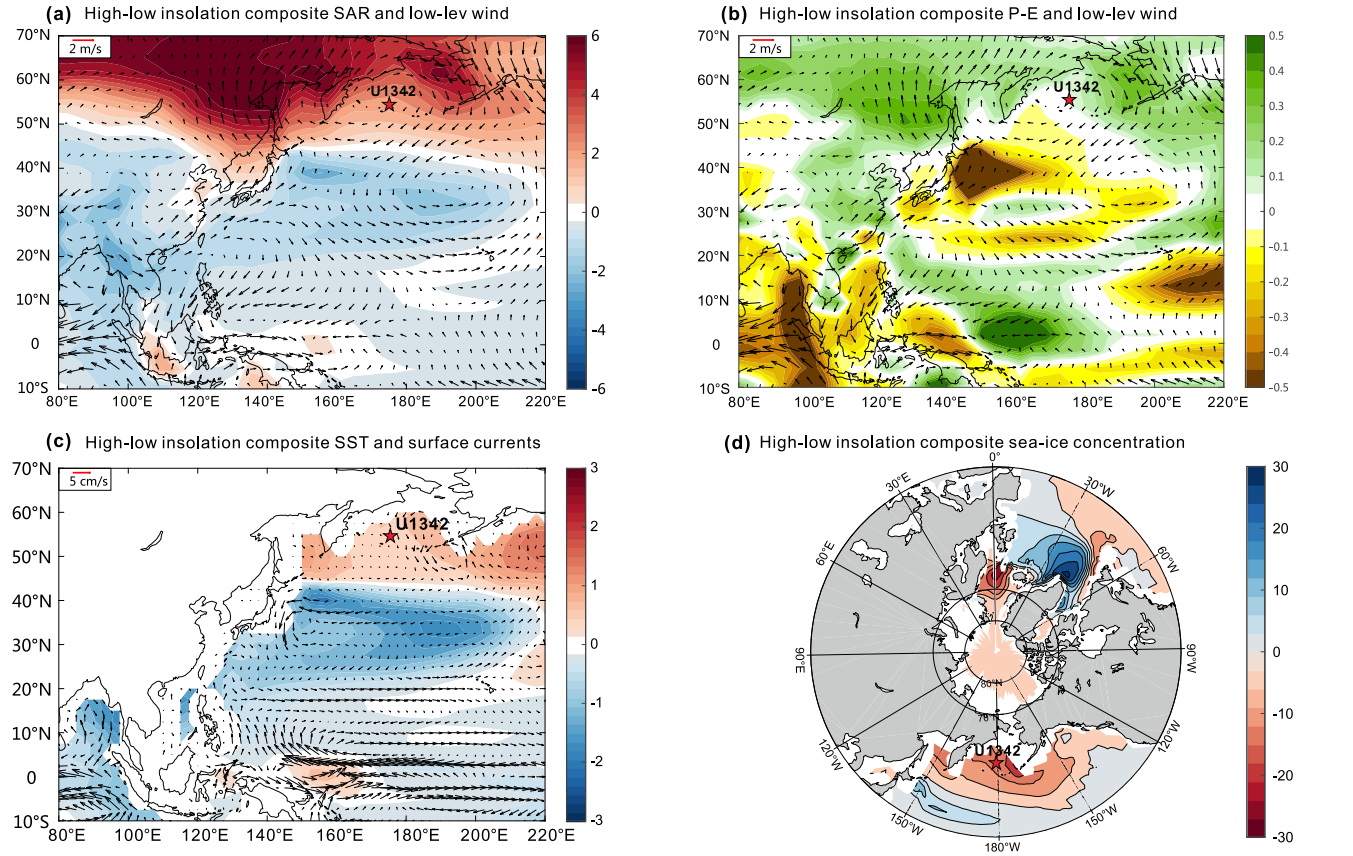

Fig. 4 | Simulated differences between precession minima and maxima (P_{min} minus P_{max}). The precession minima (maxima) are defined as the mean of six 1-kyr intervals at 60°N when summer insolation reached a maximum (minimum) since 300 ka (Supplementary Fig. 9). **a** annual mean Surface Air Temperature (SAT) and low-level (850–1000 hPa) wind (arrows), **b** annual mean precipitation minus evaporation (P-E) and low-level (850–1000 hPa) wind, and **c** annual mean Sea Surface Temperature (SST) and oceanic surface currents, and **d** annual mean Arctic sea-ice concentrations.

the high-latitude Arctic may also amplify precession-related climate changes through changes in sea-ice and snow albedo, as well as the poleward transport of heat and moisture[44–46].

Furthermore, we propose a teleconnection of orbital-scale climate variations between low and high latitudes in the North Pacific caused by a reorganization of atmospheric circulation associated with variations of the westerly jet[9]. This idea is based on recent observations showing that the large-scale ocean gyres are shifting poleward during the past few decades[47]. Their meridional displacement is influenced by a poleward shift of the strong mid-latitude westerlies in both hemispheres[48]. Transient model simulations for the SANP area show that minima in precession (or high boreal summer insolation) are the main driver of the enhancement and poleward displacement of the westerlies[49] (Fig. 2g). Moreover, expansion of the NPSG, indicated by increased oceanic heat transport between the equator and 30°N in the Pacific basin (Supplementary Figs. 4–6), is an additional factor contributing to exceptionally enhanced warmth in high-latitude regions[50–52]. With Pacific Ocean storm tracks positioned farther northward, moisture transport is enhanced in regions of higher elevation and latitude in western North America[53,54].

To test our hypothesis and to characterize the dynamics of how tropical and extratropical ocean-atmosphere systems have responded to changes in orbital parameters, we conducted a transient climate model simulation covering the last 300 kyr (see Methods for detailed information) (Fig. 4). Climate model composites during precession maxima and minima show distinct changes in temperature and precipitation, associated with changes in the general atmospheric and oceanic circulation (Fig. 4 and Supplementary Figs. 4–6). The hydroclimate response to precession at high latitudes in the Northern Hemisphere is linked to an decreased meridional temperature gradient, such as surface air temperature (SAT) and sea surface temperature (SST) (Fig. 4a). As a result, the Hadley Circulation intensifies and extends poleward (Supplementary Fig. 5), accompanied by increased precipitation, particularly in the warm pool region and in a region extending from the Asian monsoon margin to the Arctic Ocean (Fig. 4b). North Pacific Ocean gyres, primarily the North Equatorial Current, are stronger and extend northward, along with atmospheric circulation changes that favor poleward ocean heat transport, particularly in the NPSG region (Fig. 4c; Supplementary Fig. 6)[55]. Moreover, the poleward atmospheric heat transport intensified, supplied by both the upper Hadley circulation with an anomaly center around 30°N at 200 hPa, and the associated lower Ferrel circulation that is most visible around 50°N and below 850 hPa (Supplementary Fig. 5). This leads to accumulated moist static energy (MSE) in the SANP (Supplementary Fig. 7). Enhanced NPSG circulation would influence the western North American Ice sheet through the Alaska Current, which is the key conduit for northward heat transport from the NPSG to the Gulf of Alaska[56,57]. Furthermore, Arctic sea-ice volume is influenced dynamically and thermodynamically by several processes such as basal growth, frazil growth, snow-ice conversion, and basal, top, and lateral melt[58,59]. In turn, these processes influence sea-ice formation in the Pacific sector of the Arctic Ocean and Bering Sea (Fig. 4d). Note that on a global scale, in the subarctic the northward heat transport contributed by increased atmospheric heat transport although weakened by decreased ocean heat transport (Supplementary Fig. 6) can still drive increased MSE due to Bjerkness compensation[58], and provides favorable conditions for enhanced Arctic sea-ice melting. These findings reinforce our data-driven interpretation that heat and moisture transported from lower latitudes in the North

Pacific Ocean affected Arctic sea-ice melt and river discharge, as recorded in the Bering Sea sediments[32].

Precession-paced, enhanced poleward transport of heat and moisture from the low latitudes has also been observed in the Holocene records from the North Atlantic[60,61]. Thus, increased insolation occurred between 9000 and 5000 years ago driven by Earth's axial tilt, which was closer to the maximum obliquity. The precession cycle positioning the Northern Hemisphere perihelion during its summer months had a profound impact on the climate in the North Atlantic Ocean. The North Atlantic Current extended further north than today, the Atlantic Meridional Overturning Circulation (AMOC) was stronger[60,61] and sea ice sourced from the Arctic Ocean was less abundant south of Greenland[62]. Around 5000 years ago, the precession cycle led to decreased summer insolation in the Northern Hemisphere, inducing increased sea ice formation in the Arctic Ocean and export along the East Greenland coast[63,64]. At the same time, the Greenland Ice sheet began to expand[65]. These observations support the scenario put forward by our model and proxy records. Given that the transport of heat and moisture from the NPSG to the Arctic is influenced by precession-driven meridional temperature gradients, projections for future Arctic climate are highly sensitive to subpolar and extratropical SST changes (Fig. 3).

Implications for Arctic sea-ice evolution

Sea ice is a key component of Earth's climate system, with its waxing and waning are influenced by poleward moisture and heat transport[66]. Spectral analysis of our model simulation reveals that the hydroclimatic evolution of the North Pacific Ocean, as represented by seasonal precipitation, is forced by precession (Supplementary Fig. 8). This high insolation signal extends from the major monsoon regions in North Africa and Eurasia, particularly along the monsoon's northern margins, all the way to the North Pacific (Supplementary Fig. 8). Using both proxy (Fig. 2) and model data (Fig. 4) we have showed that under precession forcing, the Arctic climate is influenced by the magnitude of water vapor and latent heat transport from the mid-latitude oceans. Increased inflow of low-salinity Pacific water through the Bering Strait, combined with elevated heat discharge of pan-Arctic rivers, could also contribute to a reduction in sea-ice cover and alter the surface circulation patterns in the Arctic Ocean[67]. As a result, this anomalous, precession-paced, warm moisture is believed to play a dominant role in Arctic sea-ice formation.

Moisture delivery is also thought to be critical for ice sheet growth, even during periods such as the Last Glacial Maximum[68]. Indeed our study supports the hypothesis that low latitude processes were instrumental in shaping high-latitude glaciation and influencing global ice volume during the Pleistocene. The atmospheric and oceanic circulations with their associated heat transported the required moisture poleward. With ongoing global warming, the air above the Arctic Ocean will become warmer due to reduced Arctic sea ice cover, increasing the moisture content of the atmosphere and, thus, the atmospheric transport of sensible and latent heat to continental interiors[69]. Poleward transport of heat in the North Pacific is projected to further enhance Arctic Sea ice loss and accelerate global warming through the Arctic amplification[70–74] with potentially wide-ranging impacts on altered weather patterns and disrupted ecosystems.

Methods

Age model

Sediment cores from IODP Site U1342 (54.83°N, 176.92°E, 818 m) were sampled at ~ 3 cm intervals, yielding an average sampling frequency of one per/kyr. The age model for Site U1342 was created by visually tuning (13 tie points) the benthic foraminiferal $\delta^{18}O$ record from this site[75] (Supplementary Fig. 2c) to the global benthic LR04 $\delta^{18}O$ stack[76] (Supplementary Fig. 2a), and therefore, these records can be compared with each other[75]. Based on this age model, the depth interval between 0.045 meters below seafloor common depth (mcd) and 14.795 mcd at Site U1342 spans from 0 to 400 ka. Sedimentation rates for the selected time interval average 3.62 cm/kyr, varying between ~2.05 and ~6.32 cm/kyr (Supplementary Fig. 2c).

Diffuse reflectance spectroscopy analysis

Diffuse reflectance spectroscopy (DRS) was done with a Cary 5000 ultraviolet-visible-infrared spectrometer with $BaSO_4$ as the white standard. The scan rate was 300 nm/min from 300 to 2600 nm in 0.5 nm steps. DRS data were first transformed into the K-M remission function ($F(R) = (1-R)2/2R$, with R indicating the reflectance), and the second derivative curves of $F(R)$ were calculated following Scheinost et al. [77] and Torrent et al. [78]. Characteristic bands in these curves located at approximately 535 and 425 nm represent pure hematite and goethite, respectively[77,78]. The corresponding band intensities for hematite and goethite are defined as I_{Hm} and I_{Gt}, which are proportional to the concentration of hematite and goethite[78].

Clay mineral analysis

A total of 123 samples from Site U1342 were analysed for their clay mineralogy using X-ray diffraction (XRD). Clay minerals in the <2 µm fraction were separated by settling according to Stokes law after the removal of organic matter and carbonate by treatment with hydrogen peroxide (15%) and acetic acid (10%). The clay minerals were analysed by XRD using a Bruker D8 Advance diffractometer with CuKα radiation (40 kV, 40 mA) at the Qingdao Sparta Analysis & Test Co., Ltd, China. Identification of clay minerals was made according to the position of the (001) series of basal reflections on the ethylene glycol XRD diagram[79]. Clay mineral abundances were semi-quantitatively estimated based on the peak areas of the basal reflection for the major clay mineral groups (smectite: 17 Å, illite: 10 Å, and kaolinite/chlorite: 7 Å). We used the JADE 6.5 software with the empirical factors of Biscaye[80]. The residual error of each sample's fitting is less than 8%.

Time series analysis

Multi-taper analysis (MTM) and evolutionary Fast Fourier Transform (eFFT)[81] were applied to determine frequency changes and major astronomical periods in the respective variables using the Acycle v2.6 open source software[82]. Before spectral analysis, the raw data were standardized. The 35% weighted average long-term trend was removed by using a "LOWESS" preprocessing method[83]. The multi-taper method spectral estimator was employed to analyse the series data after linear trend removal with 2π tapers[84]. The average, 90%, 95%, and 99% confidence levels of the resulting spectral peaks were calculated using robust AR (1) noise models[85]. The 23-kyr precession cyclicity in the goethite record was extracted by a bandpass filter, set at frequencies from 0.040 to 0.046 (1/kyr). The target frequencies utilized in this study were obtained from Laskar et al. [38].

Collection of existing palaeoclimatic records

Numerous palaeoclimatic records spanning orbital scales have been documented at all latitudes in the North Pacific and monsoon regions. In this study, we compiled 22 published records that were primarily precession forced (Supplementary Table 1). These records represent the overall spatial distribution pattern of precession forced conditions during orbital timescales ranging from 2°S to 83°N in the North Pacific Ocean.

Climate model and experiment design

The fully coupled NCAR-CCSM3 model with its active atmosphere, land, ocean, and sea ice components was employed in this work. This model has a spatial resolution of 3.75° for the atmosphere (26 vertical layers) and land, a variable latitudinal resolution (~ 0.9° near the equator, coarser poleward), and a longitudinal resolution of ~3.6° for the ocean (25 vertical layers) and sea-ice. In addition, to investigate the

East Asian monsoon rainfall response to transient orbital forcing with complete precession (~20,000-year), obliquity (~40,000-year), and eccentricity (~100,000-year) cycles[86], we analysed a transient simulation (comprising orbital (ORB)) driven by realistic orbital forcing parameters since 300 ka. ORB was initialized from a pre-industrial state. To focus on the orbital forcing alone, other boundary conditions, such as greenhouse gas concentrations and ice-sheet volume, were fixed at the pre-industrial level.

Data availability

All data needed to evaluate the conclusions in the paper are present in the paper and/or Supplementary Material. The underlying measured proxy data are available at https://doi.org/10.5281/zenodo.12792822.

Code availability

The code for Figs. 1 and 4 are available at https://doi.org/10.5281/zenodo.12792822.

References

1. Cohen, J. et al. Recent Arctic amplification and extreme mid-latitude weather. *Nat. Geosci.* **7**, 627–637 (2014).
2. Coumou, D., Di Capua, G., Vavrus, S., Wang, L. & Wang, S. The influence of Arctic amplification on mid-latitude summer circulation. *Nat. Commun.* **9**, 2959 (2018).
3. Post, E. et al. The polar regions in a 2 °C warmer world. *Sci. Adv.* **5**, eaaw9883 (2019).
4. Matsumura, S. & Kosaka, Y. Arctic–Eurasian climate linkage induced by tropical ocean variability. *Nat. Comm.* **10**, 3441 (2019).
5. Xu, G. et al. High-resolution modelling identifies the Bering Strait's role in amplified Arctic warming. *Nat. Clim. Change.* **14**, 615–622 (2024).
6. Joh, Y. & Di Lorenzo, E. Interactions between Kuroshio Extension and Central Tropical Pacific lead to preferred decadal-timescale oscillations in Pacific climate. *Sci. Rep.* **9**, 13558 (2019).
7. Zhang, Y., Zhang, Z., Chen, D., Qiu, B. & Wang, W. Strengthening of the Kuroshio current by intensifying tropical cyclones. *Science* **368**, 988–993 (2020).
8. Hu, D. et al. Pacific western boundary currents and their roles in climate. *Nature* **522**, 299–308 (2015).
9. Yang, H. et al. Intensification and poleward shift of subtropical western boundary currents in a warming climate. *J. Geophys. Res. Oceans* **121**, 4928–4945 (2016).
10. Munk, W. H. On the wind-driven ocean circulation. *J. Meteorol. Res.* **7**, 79–93 (1950).
11. Max, L. et al. Evidence for enhanced convection of North Pacific Intermediate Water to the low-latitude Pacific under glacial conditions. *Paleoceanogr. Paleoclimat.* **32**, 41–55 (2017).
12. Naidu, A. S., Han, M. W., Mowatt, T. C. & Wajda, W. Clay minerals as indicators of sources of terrigenous sediments, their transportation and deposition: Bering Basin, Russian-Alaskan Arctic. *Mar. Geol.* **127**, 87–104 (1995).
13. Liu, Q., Torrent, J., Yu, Y. & Deng, C. Mechanism of the parasitic remanence of aluminous goethite [α-(Fe, Al)OOH]. *J. Geophys. Res.-Solid Earth* **109**, B12106 (2004).
14. Maxbauer, D. P., Feinberg, J. M. & Fox, D. L. Magnetic mineral assemblages in soils and paleosols as the basis for paleoprecipitation proxies: A review of magnetic methods and challenges. *Earth-Sci. Rev.* **155**, 28–48 (2016).
15. Lund, S. et al. Rock magnetic variability of quaternary deep-sea sediments from the Bering Sea and their environmental implications. *Deep-Sea Res. Part I-Oceanogr. Res. Pap.* **172**, 103487 (2021).
16. Lund, S., Okada, M. & Mortazavi, E. Paleomagnetic secular variation and revised chronostratigraphy of Bering Sea (IODP expedition 323) deep-sea sediments (MIS 5). *Deep-Sea Res. Part I-Oceanogr. Res. Pap.* **208**, 104265 (2024).
17. Yiou, P., Ghil, M., Jouzel, J., Paillard, D. & Vautard, R. J. C. D. Nonlinear variability of the climatic system from singular and power spectra of Late Quaternary records. *Clim. Dyn.* **9**, 371–389 (1994).
18. Liu, J., Fang, N., Wang, F., Yang, F. & Ding, X. J. P. Features of ice-rafted debris (IRD) at IODP site U1312 and their palaeoenvironmental implications during the last 2.6 Myr. *Paleogeog. Paleoclimatol. Paleoecol.* **511**, 364–378 (2018).
19. Bahr, A., Catunda, M. C. A. & Friedrich, O. The first appearance of Glacial North Atlantic Intermediate Water (GNAIW) during the Mid-Pleistocene transition. *Glob. Planet. Change* **218**, 103977 (2022).
20. Marzen, R. E., DeNinno, L. H. & Cronin, T. M. Calcareous microfossil-based orbital cyclostratigraphy in the Arctic Ocean. *Quat. Sci. Rev.* **149**, 109–121 (2016).
21. Jakobsson, M. et al. Evidence for an ice shelf covering the central Arctic Ocean during the penultimate glaciation. *Nat. Comm.* **7**, 10365 (2016).
22. Berger, A., Yin, Q. & Wu, Z. Length of astronomical seasons, total and average insolation over seasons. *Quat. Sci. Rev.* **334**, 108620 (2024).
23. Wu, Z., Yin, Q., Guo, Z. & Berger, A. Hemisphere differences in response of sea surface temperature and sea ice to precession and obliquity. *Glob. Planet. Change* **192**, 103223 (2020).
24. Vats, N., Mishra, S., Singh, R. K., Gupta, A. K. & Pandey, D. K. Paleoceanographic changes in the East China Sea during the last ~400 kyr reconstructed using planktic foraminifera. *Glob. Planet. Change* **189**, 103173 (2020).
25. Zhao, D. et al. Quaternary rainfall variability is governed by insolation in northern China and ice-sheet forcing in the South. *Commun. Earth Environ.* **4**, 7 (2023).
26. Zhao, D. et al. Response of heterogeneous rainfall variability in East Asia to Hadley circulation reorganization during the late Quaternary. *Quat. Sci. Rev.* **247**, 106562 (2020).
27. Cheng, H. et al. The Asian monsoon over the past 640,000 years and ice age terminations. *Nature* **534**, 640–646 (2016).
28. Cheng, H. et al. Eastern North American climate in phase with fall insolation throughout the last three glacial-interglacial cycles. *Earth Planet. Sci. Lett.* **522**, 125–134 (2019).
29. Lachniet, M. S., Denniston, R. F., Asmerom, Y. & Polyak, V. J. Orbital control of western North America atmospheric circulation and climate over two glacial cycles. *Nat. Comm.* **5**, 3805 (2014).
30. Berger, A. L. Long-term variations of dailty insolation and Quaternary climatic changes. *J. Atmos. Sci.* **35**, 2362–2367 (1978).
31. Zhong, Y. et al. Paleoclimate evolution of the North Pacific Ocean during the late Quaternary: Progress and challenges. *Geochem. Geoenviron.* **2**, 100124 (2023).
32. Zhong, Y. et al. Coupled Impacts of Atmospheric Circulation and Sea-Ice on Late Pleistocene Terrigenous Sediment Dynamics in the Subarctic Pacific Ocean. *Geophys. Res. Lett.* **48**, e2021GL095312 (2021).
33. Laepple, T. & Lohmann, G. J. P. Seasonal cycle as template for climate variability on astronomical timescales. *Paleoceanography* **24**, PA4201 (2009).
34. Kaboth-Bahr, S. et al. Paleo-ENSO influence on African environments and early modern humans. *Proc. Natl. Acad. Sci.* **118**, e2018277118 (2021).
35. Schaebitz, F. et al. Hydroclimate changes in eastern Africa over the past 200,000 years may have influenced early human dispersal. *Comm. Earth Environ.* **2**, 123 (2021).
36. Abe-Ouchi, A. et al. Insolation-driven 100,000-year glacial cycles and hysteresis of ice-sheet volume. *Nature* **500**, 190–193 (2013).
37. Clark, P. U., Shakun, J. D., Rosenthal, Y., Köhler, P. & Bartlein, P. J. Global and regional temperature change over the past 4.5 million years. *Science* **383**, 884–890 (2024).
38. Laskar, J. et al. long-term numerical solution for the insolation quantities of the Earth. *Astron. Astrophys.* **428**, 261–285 (2004).

39. Xiao, W. et al. Middle to Late Pleistocene Arctic paleoceanographic changes based on sedimentary records from Mendeleev Ridge and Makarov Basin. *Quat. Sci. Rev.* **228**, 106105 (2020).
40. Adler, R. E. et al. Crawford, Sediment record from the western Arctic Ocean with an improved Late Quaternary age resolution: HOTRAX core HLY0503-8JPC, Mendeleev Ridge. *Glob. Planet. Change* **68**, 18–29 (2009).
41. O'Regan, M. et al. Constraints on the Pleistocene chronology of sediments from the Lomonosov Ridge. *Paleoceanography* **23**, PA1S19 (2008).
42. Wang, R. et al. Late-Middle Quaternary lithostratigraphy and sedimentation patterns on the Alpha Ridge, central Arctic Ocean: Implications for Arctic climate variability on orbital time scales. *Quat. Sci. Rev.* **181**, 93–108 (2018).
43. Hao, Q. et al. Delayed build-up of Arctic ice sheets during 400,000-year minima in insolation variability. *Nature* **490**, 393–396 (2012).
44. Jackson, C. S. & Broccoli, A. J. Orbital forcing of Arctic climate: mechanisms of climate response and implications for continental glaciation. *Clim. Dyn.* **21**, 539–557 (2003).
45. Khodri, M., Cane, M. A., Kukla, G., Gavin, J. & Braconnot, P. The impact of precession changes on the Arctic climate during the last interglacial–glacial transition. *Earth Planet. Sci. Lett.* **236**, 285–304 (2005).
46. Guo, D. et al. Mechanism on how the spring Arctic sea ice impacts the East Asian summer monsoon. *Theor. Appl. Climatol.* **115**, 107–119 (2014).
47. Hu, Y. et al. Poleward shift of the major ocean gyres detected in a warming climate. *Geophys. Res. Lett.* **47**, e2019GL085868 (2020).
48. Saenko, Q. A., Fyfe, J. C. & England, M. H. On the response of the oceanic wind-driven circulation to atmospheric CO_2 increase. *Clim. Dyn.* **25**, 415–426 (2005).
49. Yao, Z. et al. Ice sheet and precession controlled subarctic Pacific productivity and upwelling over the last 550,000 years. *Nat. Commun.* **15**, 3489 (2024).
50. Nishikawa, H., Nishikawa, S., Ishizaki, H., Wakamatsu, T. & Ishikawa, Y. J. P. I. E. Detection of the Oyashio and Kuroshio fronts under the projected climate change in the 21st century. *Science* **7**, 1–12 (2020).
51. Sakamoto, T. T. et al. Responses of the Kuroshio and the Kuroshio Extension to global warming in a high-resolution climate model. *Geophys. Res. Lett.* **32**, L14617 (2005).
52. Taylor, S. P. et al. Expanded north pacific subtropical gyre and heterodyne expression during the Mid-Pleistocene. *Paleoceanogr. Paleoclimatol.* **37**, e2021PA004395 (2022).
53. Shaw, T. A. et al. Storm track processes and the opposing influences of climate change. *Nat. Geosci.* **9**, 656–664 (2016).
54. Wise, E. K. & Dannenberg, M. P. Reconstructed storm tracks reveal three centuries of changing moisture delivery to North America. *Sci. Adv.* **3**, e1602263 (2017).
55. McGee, D., Donohoe, A., Marshall, J. & Ferreira, D. Changes in ITCZ location and cross-equatorial heat transport at the Last Glacial Maximum, Heinrich Stadial 1, and the mid-Holocene. *Earth Planet. Sci. Lett.* **390**, 69–79 (2014).
56. Jacox, M. G., Fiechter, J., Moore, A. M. & Edwards, C. A. ENSO and the California Current coastal upwelling response. *J. Geophys. Res. Oceans* **120**, 1691–1702 (2015).
57. Jacox, M. G., Moore, A. M., Edwards, C. A. & Fiechter, J. Spatially resolved upwelling in the California Current System and its connections to climate variability. *Geophys. Res. Lett.* **41**, 3189–3196 (2014).
58. Lee, Y. C. et al. Impacts of Atlantic meridional overturning circulation weakening on Arctic amplification. *Proc. Natl. Acad. Sci.* **121**, e2402322121 (2024).
59. Lee, Y. C. & Liu, W. The weakened atlantic meridional overturning circulation diminishes recent arctic sea ice loss. *Geophys. Res. Lett.* **50**, e2023GL105929 (2023).
60. Risebrobakken, B. et al. Early Holocene temperature variability in the Nordic Seas: The role of oceanic heat advection versus changes in orbital forcing. *Paleoceanography* **26**, PA4206 (2011).
61. Wang, R. Mechanisms for low-frequency variability of summer Arctic sea ice extent. *Proc. Natl. Acad. Sci.* **112**, 4570–4575 (2015).
62. Liu, W., Fedorov, A. V., Xie, S. P. & Hu, S. Climate impacts of a weakened Atlantic Meridional Overturning Circulation in a warming climate. *Sci. Adv.* **6**, eaaz4876 (2020).
63. Andresen, C., Sha, S. L., Seidenkrantz, M. S., Dyke, L. & Jiang, M. H. Early Holocene palaeoceanographic and glaciological changes in southeast Greenland. *Holocene* **32**, 501–514 (2022).
64. Perner, K., Moros, M., Lloyd, J. M., Janse, E. & Stein, R. Mid to late Holocene strengthening of the East Greenland Current linked to warm subsurface Atlantic water. *Quat. Sci. Rev.* **129**, 296–307 (2015).
65. Jennings, A. E., Kudsen, K. L., Hald, M., Hanse, C. V. & Andrew, J. T. A mid-Holocene shift in Arctic sea-ice variability on the East Greenland Shelf. *Holocene* **12**, 49–58 (2002).
66. Catunda, M. C. et al. Subsurface heat channel drove sea surface warming in the high-latitude north Atlantic during the mid-Pleistocene transition. *Geophys. Res. Lett.* **48**, e2020GL091899 (2021).
67. Woodgate, R. A. Increases in the Pacific inflow to the Arctic from 1990 to 2015, and insights into seasonal trends and driving mechanisms from year-round Bering Strait mooring data. *Prog. Oceanogr.* **160**, 124–154 (2018).
68. Halberstadt, A. R. W. et al. CO_2 and tectonic controls on Antarctic climate and ice-sheet evolution in the mid-Miocene. *Earth Planet. Sci. Lett.* **564**, 116908 (2021).
69. Huang, Y. et al. Thicker Clouds and Accelerated Arctic Sea Ice Decline: The Atmosphere-Sea Ice Interactions in Spring. *Geophys. Res. Lett.* **46**, 6980–6989 (2019).
70. Lindsay, R. & Schweiger, A. Arctic sea ice thickness loss determined using subsurface, aircraft, and satellite observations. *Cryosphere* **9**, 269–283 (2015).
71. Notz, D. & Stroeve, J. Observed Arctic sea-ice loss directly follows anthropogenic CO2 emission. *Science* **354**, 747–750 (2016).
72. Olonscheck, D., Mauritsen, T. & Notz, D. Arctic sea-ice variability is primarily driven by atmospheric temperature fluctuations. *Nat. Geosci.* **12**, 430 (2019).
73. Ballantyne, A. P. et al. The amplification of Arctic terrestrial surface temperatures by reduced sea-ice extent during the Pliocene. *Paleogeogr. Paleoclimatol. Paleoecol.* **386**, 59–67 (2013).
74. Jansen, E. et al. Past perspectives on the present era of abrupt Arctic climate change. *Nat. Clim. Change* **10**, 714–721 (2020).
75. Knudson, K. P. & Ravelo, A. C. North Pacific Intermediate Water circulation enhanced by the closure of the Bering Strait. *Paleoceanography* **30**, 1287–1304 (2016).
76. Lisiecki, L. E. & Raymo, M. E. A Pliocene-Pleistocene stack of 57 globally distributed benthic $\delta^{18}O$ records. *Paleoceanography* **20**, PA1003 (2005).
77. Scheinost, A. C. et al. Use and limitations of second-derivative diffuse reflectance spectroscopy in the visible to near-infrared range to identify and quantify Fe oxide minerals in soils. *Clay Clay Min* **46**, 528–536 (1998).
78. Torrent, J., Liu, Q., Bloemendal, J. & Barron, V. Magnetic enhancement and iron oxides in the upper luochuan Loess-paleosol sequence, Chinese Loess plateau. *Soil Sci. Soc. Am. J.* **71**, 1570–1578 (2007).
79. Moore, D. M. & Reynolds, R. C. X-Ray diffraction and the identification and analysis of clay minerals. Oxford University Press (1989).
80. Biscaye, P. E. Mineralogy and sedimentation of recent deep-sea clay in the Atlantic Ocean and adjacent seas and oceans. *Geol. Soc. Am. Bull.* **76**, 803–832 (1965).

81. Kodama, K. P. & Hinnov, L. A. Rock magnetic cyclostratigraphy. John Wiley & Sons (2014).
82. Li, M., Hinnov, L. & Kump, L. Acycle: Time-series analysis software for paleoclimate research and education. *Comput. Geosci.* **127**, 12–22 (2019).
83. Cleveland, W. S. Robust locally weighted regression and smoothing scatterplots. *J. Am. Stat. Assoc.* **74**, 829–836 (1979).
84. Thomson, D. J. Spectrum estimation and harmonic analysis. *Proc. IEEE* **70**, 1055–1096 (1982).
85. Mann, M. E. & Lees, J. M. Robust estimation of background noise and signal detection in climatic time series. *Clim. Change* **33**, 409–445 (1996).
86. Berger, A. & Loutre, M. F. 1991. Insolation values for the climate of the last 10,000,000 Years. *Quat. Sci. Rev.* **10**, 297–317 (1991).
87. Kanamitsu, M. et al. NCEP-DOE AMIP-II reanalysis (R-2). *Bull. Amer. Meteorol. Soc.* **83**, 1631–1643 (2002).
88. Walczak et al. Phasing millennial-scale climate variability in the Pacific and Atlantic Oceans. *Science* **370**, 716–720 (2020).
89. Morley, J. J. & Heusser, L. E. Role of orbital forcing in east Asian monsoon climates during the last 350 kyr: Evidence from terrestrial and marine climate proxies from core RC14-99. *Paleoceanography* **12**, 483–493 (1997).
90. Yamamoto, M. Response of mid-latitude North Pacific surface temperatures to orbital forcing and linkage to the East Asian summer monsoon and tropical ocean–atmosphere interactions. *J. Quat. Sci.* **24**, 836–847 (2009).
91. Zou, J. et al. Sedimentary mercury and antimony revealed orbital-scale dynamics of the Kuroshio Current. *Quat. Sci. Rev.* **265**, 107051 (2021).
92. Thomas, E. K. et al. Temperature and leaf wax δ^2H records demonstrate seasonal and regional controls on Asian monsoon proxies. *Geology* **42**, 1075–1078 (2014).
93. Zhang, Y. G., Ji, J., Balsam, W. L., Liu, L. & Chen, J. High resolution hematite and goethite records from ODP 1143, South China Sea: Co-evolution of monsoonal precipitation and El Niño over the past 600,000 years. *Earth Planet. Sci. Lett.* **264**, 136–150 (2007).
94. Tachikawa, K. et al. The precession phase of hydrological variability in the Western Pacific Warm Pool during the past 400 ka. *Quat. Sci. Rev.* **30**, 3716–3727 (2011).
95. Sun, Y. et al. Source-to-sink fluctuations of Asian eolian deposits since the late Oligocene. *Earth Sci. Rev.* **200**, 102963 (2019).
96. Guo, B. H. et al. Dominant precessional forcing of the East Asian summer monsoon since 260 ka. *Geology* **50**, G50206 (2022).
97. Rohling, E. J. et al. Sea-level and deep-sea-temperature variability over the past 5.3 million years. *Nature* **508**, 477 (2014).

Acknowledgements

We would like to thank the International Ocean Drilling Program and the curators at the Kochi Core Center (Japan) for providing samples. We thank Dr. Zhipeng Wu, Gaopeng Xu and Qing Yan for helpful suggestions and comments. Funding was provided by the National Natural Science Foundation of China (grant 42261144739, 42274094, 42176245, 92158208, 42304082 and 42330403), Shenzhen Science and Technology Program (JCYJ20240813094216022, KCXFZ20211020174803005) and the High Level Special Fund of SUSTech (G0305K001), The Science and Technology Innovation Project of Laoshan Laboratory (project number LSKJ202204203). Z.L. is supported by the Swedish Research Council Vetenskapsrådet (Grant No. 2022-03617) and the Swedish Research Council Formas (Grant No. 2020-02267). The 300-ka transient simulation was processed and analysed on resources provided by the National Academic Infrastructure for Supercomputing in Sweden (NAISS) at Linköping University. X.W. acknowledges the financial support from the Singapore Ministry of Education under grant number MOE-MOET32022-0006.

Author contributions

Y.Z., and Q.S.L. designed the project. Y.Z., S.K.B., J.M.Y., K.H., M.J.D., J.C.L., P.D.C., M.E.W., F.V., S.K., X.F.W., C.S.A., H.W.Z., X.G.F., and D.B.Z. prepared the first draft of the manuscript. Y.G.L., Z.Y.D., J.Y.Z., W.Y.X., and S.Y. completed the sample collection. Z.Y.D. was responsible for sample preparation. W.Y.X. and H.L were responsible for data collection and/or synthesis. Z.L. analysed climate simulation and reanalysis data. C.J.S., H.Y., L.N. assisted with model simulations.

Competing interests

The authors declare no competing interests.

Additional information

Supplementary information The online version contains supplementary material available at https://doi.org/10.1038/s41467-025-56542-1.

Correspondence and requests for materials should be addressed to Yi Zhong, Zhengyao Lu or Qingsong Liu.

Peer review information *Nature Communications* thanks the anonymous reviewers for their contribution to the peer review of this work. A peer review file is available.

Reprints and permissions information is available at http://www.nature.com/reprints

Publisher's note Springer Nature remains neutral with regard to jurisdictional claims in published maps and institutional affiliations.

Open Access This article is licensed under a Creative Commons Attribution-NonCommercial-NoDerivatives 4.0 International License, which permits any non-commercial use, sharing, distribution and reproduction in any medium or format, as long as you give appropriate credit to the original author(s) and the source, provide a link to the Creative Commons licence, and indicate if you modified the licensed material. You do not have permission under this licence to share adapted material derived from this article or parts of it. The images or other third party material in this article are included in the article's Creative Commons licence, unless indicated otherwise in a credit line to the material. If material is not included in the article's Creative Commons licence and your intended use is not permitted by statutory regulation or exceeds the permitted use, you will need to obtain permission directly from the copyright holder. To view a copy of this licence, visit http://creativecommons.org/licenses/by-nc-nd/4.0/.

© The Author(s) 2025

[1]Centre for Marine Magnetism (CM2, Department of Ocean Science and Engineering, Southern University of Science and Technology, Shenzhen 518055, China. [2]Advanced Institute of Ocean Research, Department of Ocean Scicence and Engineering, Southern University of Science and Technology, Shenzhen 518055, China. [3]Department of Physical Geography and Ecosystem Science, Lund University, Lund, Sweden. [4]Nanjing-Helsinki Institute in Atmospheric and Earth System Sciences, Nanjing University, Nanjing 210023, China. [5]Institute of Geological Sciences, Frei Universität Berlin, 12249 Berlin, Germany. [6]Laoshan Laboratory, Qingdao, China. [7]Research School of Earth Sciences, Australian National University, Canberra, ACT, Australia. [8]SKLLQG, Institute of Earth

Environment, Chinese Academy of Sciences, Xi' an, China. [9]Faculty of Science, Academic Assembly, University of Toyama, Toyama, Japan. [10]Paleomagnetic Laboratory 'Fort Hoofddijk', Department of Earth Sciences, Faculty of Geosciences, Utrecht University, Utrecht, The Netherlands. [11]Departamento de Ciencias, Universidad Pública de Navarra, Campus de Arrosadia, 31006 Pamplona, Spain. [12]IGME, CSIC, Campus Aula Dei, 50059 Zaragoza, Spain. [13]Department of Earth Sciences, University College London, London WC1E 6BS, UK. [14]Institute for Geosciences, Department of Geochemistry and Petrology, University of Bonn, Bonn, Germany. [15]Department of Geological Sciences, Stockholm University, Stockholm, Sweden. [16]Camborne School of Mines, Department of Earth and Environment Sciences, University of Exeter, Cornwall, UK. [17]Department of Earth and Planetary Sciences, University of California Davis, Davis, CA 95616, USA. [18]Southern Marine Science and Engineering Guangdong Laboratory (Zhuhai), Zhuhai, China. [19]Earth Observatory of Singapore and Asian School of the Environment, Nanyang Technological University, Singapore 639798, Singapore. [20]Geological Survey of Denmark and Greenland, Department of Glaciology and Climate, Øster Voldgade10, 1350, Copenhagen K, Denmark. [21]Key Laboratory of Marine Geology and Metallogeny, First Institute of Oceanography, Ministry of Natural Resources (MNR), Qingdao 266061, China. [22]College of Ocean Science and Engineering, Shandong University of Science and Technology, Qingdao, China. [23]Institute of Global Environmental Change, Xi'an Jiaotong University, Xi'an 710054, China. [24]Alfred-Wegener-Institut Helmholtz-Zentrum für Polar- und Meeresforschung, Bremerhaven, Germany. [25]Key Laboratory of Marine Geology and Environment, Institute of Oceanology, Chinese Academy of Sciences, Qingdao 266071, China. [26]Southern Marine Science and Engineering Guangdong Laboratory (Guangzhou), Guangzhou 511458, China. [27]Shanghai Sheshan National Geophysical Observatory, Shanghai, China. ✉e-mail: zhongy@sustech.edu.cn; zhengyao.lu@nateko.lu.se; qsliu@sustech.edu.cn